Received: 13 January 2026 | Revised: 14 April 2026 | Accepted: 22 June 2026 | Published online: 16 July 2026

RESEARCH ARTICLE

Journal of Optics and Photonics Research
2026, Vol. 00(00) 1–8
DOI: 10.47852/bonviewJOPR62029098

BON VIEW PUBLISHING

Band-Structure Engineering of P-Doped Ge/SiGe Heterostructures for Mid-infrared Photonic Devices

Vittoria Urso[1,*]

[1] *Department of Physics "Enrico Fermi", University of Pisa, Italy*

Abstract: This work presents a systematic theoretical investigation and band-structure engineering of p-doped Ge/$Si_{1-x}Ge_x$ multiple quantum wells (MQWs) tailored for mid-infrared (MIR) photonics. Using a self-consistent 6-band k · p Poisson-Schrödinger approach, we establish a predictive simulation framework that rigorously accounts for quantum confinement, epitaxial strain, and many-body interactions. A key feature of our model is the integration of realistic graded interfacial profiles and self-consistent many-body corrections—specifically local density approximation exchange—correlation and depolarization shifts. We demonstrate that these corrections are essential to resolve the observed 8–12 meV energy blueshift in high-density hole gases (> $10^{18} cm^{-3}$), where standard single-particle approximations fail. By systematically optimizing well geometry, doping profiles, and Ge concentration, we achieve precise spectral tunability across the strategic 6–15 μm atmospheric window. Furthermore, our transport and optical models capture the complex valence band mixing between heavy, light, and split-off hole states, providing deep insights into intersubband absorption dynamics. The model's high predictive accuracy (> 95% compared to experimental MIR absorption spectra) establishes it as an indispensable tool for the ab-initio design of CMOS-compatible MIR emitters, quantum cascade lasers, and photodetectors. Ultimately, this framework bridges the gap between fundamental valence band physics and practical device performance, accelerating the development of next-generation monolithic silicon-photonics platforms.

Keywords: quantum well infrared photodetector, SiGe heterostructures, mid-infrared, strain engineering, numerical simulation

1. Introduction

The mid-infrared (MIR) spectral range, particularly the "fingerprint" region (6−15 μm), represents a frontier for integrated photonics, offering unparalleled opportunities for molecular spectroscopy [1, 2], environmental monitoring [3–7], and medical diagnostics [8–10]. Among the competing material platforms, Ge-rich SiGe heterostructures have emerged as a leading candidate due to their CMOS compatibility [11–14] and the wide transparency window of Germanium [3, 15–18]. However, as the field transitions from passive waveguiding [19, 20] to active optoelectronic components like Quantum Well Infrared Photodetectors (QWIPs) [21, 22] and modulators [23, 24], the need for precise band-structure engineering becomes paramount. Intersubband transitions (ISBTs) in hole-doped Ge/SiGe MQWs are particularly attractive because the valence band offers significantly larger offsets (up to 300 meV) compared to the conduction band, enabling devices to operate across the entire MIR spectrum. Despite these advantages, the valence band complexity characterized by the strong coupling between heavy-hole (HH), light-hole (LH), and split-off (SO) bands [25–27] presents a significant challenge for device design. The performance of these heterostructures is highly sensitive to strain-induced shifts, quantum confinement, and many-body effects [28, 29], which cannot be fully captured by simplified analytical models. While recent experimental works [30] have successfully demonstrated the growth and basic optical response of p-doped Ge/SiGe MQWs, a comprehensive theoretical framework is required to explore the vast parameter space that epitaxial growth alone cannot efficiently probe. Unlike simplified effective mass models (e.g., in the work by Lodari et al. [26]), which often neglect non-parabolicity and many-body renormalization, our 6-band $k \cdot p$ approach captures the fine structure of the hole dispersion and the redistribution of oscillator strength at high carrier densities. Furthermore, a critical yet frequently overlooked challenge in modeling these heterostructures is the impact of realistic, non-abrupt interfacial profiles. During epitaxial growth, atomic interdiffusion inevitably creates graded interfaces rather than ideal, atomistically sharp step potentials. This interface grading drastically modifies the local electrostatic potential, smooths the quantum well boundaries, and alters both the confinement energies and the spatial overlap of valence subband wave functions. When coupled with high carrier densities, these structural deviations trigger complex many-body phenomena, including local exchange-correlation effects and collective depolarization shifts, which significantly renormalize the ISBT energies. Consequently, a rigorous, self-consistent treatment that simultaneously incorporates both non-ideal structural geometry and many-body corrections is strictly mandatory to achieve

***Corresponding author:** Vittoria Urso, Department of Physics "Enrico Fermi", University of Pisa, Italy. Email: vittoria.urso@df.unipi.it

genuine predictive accuracy. In this work, we employ the Nextnano simulation suite [31] to perform a systematic study of the electronic and optical properties of p-doped Ge/SiGe MQWs. By utilizing a self-consistent $k \cdot p$ Poisson-Schrödinger solver [32], we investigate how structural variations such as well thickness, Ge concentration, and doping profiles impact the oscillator strength and the spectral linewidth of ISBTs [33]. This theoretical investigation aims to provide a predictive design suite, identifying the physical limits and optimal configurations for next-generation Si-based MIR modulators and emitters, effectively bridging the gap between fundamental semiconductor physics and practical photonic applications [34].

2. Theoretical Modeling and Computational Methods

2.1. Device architecture and interface modeling

The simulated heterostructure consists of a p-doped Ge/SiGe multiple quantum well (MQW) system designed for mid-infrared (MIR) operation. To ensure alignment with recent experimental benchmarks (Sample A and B) [30], the nominal design features 3-nm-thick Ge QWs sandwiched between 8-nm-thick $Si_{0.3}Ge_{0.7}$ barriers. The entire active region is modeled as coherently grown on a $Si_{0.2}Ge_{0.8}$ virtual substrate (VS) [26] (see Figure 1 [30]). A critical aspect of this model is the transition from idealized abrupt heterojunctions to a more realistic graded compositional profile. To account for the entropic interdiffusion and surface roughening typically observed in low-energy plasma-enhanced chemical vapor deposition (LEPECVD) [35], a self-consistent interface model was implemented. The Germanium concentration $x(z)$ across the well-barrier transitions is described by a sum of error functions:

Figure 1
Structural properties of the Ge/SiGe heterostructure

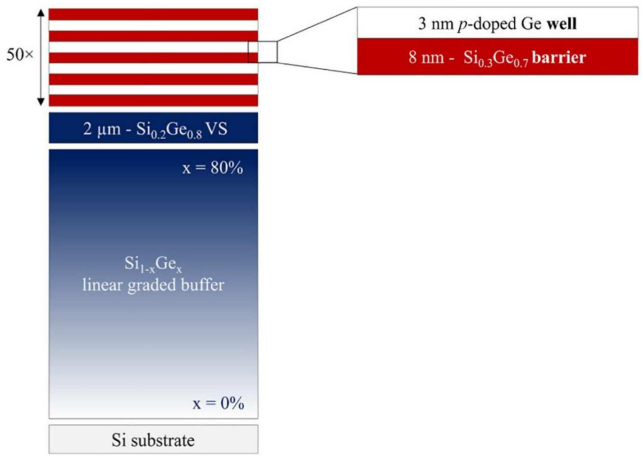

$$x(z) = x_L erf(\frac{z - z_L}{\sigma_L}) + x_R erf(\frac{z - z_R}{\sigma_R}) + x_{bg} \quad (1)$$

In this framework, the parameters σ_L and σ_R (ranging from 0.6 to 0.7 nm) define an intermixing region of approximately 1 nm at each interface. This choice of σ is physically justified by transmission electron microscopy (TEM) and secondary ion mass spectrometry (SIMS) characterizations of Ge/SiGe interfaces grown via LEPECVD at temperatures below 500 °C, which consistently exhibit atomic-scale grading due to surface segregation and limited thermal diffusion [35]. To assess the robustness of the model, a sensitivity analysis was performed by varying the intermixing parameter. We observed that shifting σ from 0.4 nm (near-abrupt) to 1.0 nm (highly diffused) induces a change in the $HH_0 \rightarrow HH_1$ transition energy of approximately 5 meV. This result confirms that a refined potential profile is essential for an accurate determination of the confinement potential and the higher-order excited states near the barrier edge, which directly govern the ISBTs and the subsequent carrier extraction in sensing devices.

2.2. Self-consistent 6-band $k \cdot p$ and strain modeling

To validate the numerical framework, simulations were performed targeting two specific doping configurations, hereafter referred to as Sample A (2.5×10^{18} cm^{-3}) and Sample B (5×10^{18} cm^{-3}), corresponding to recent experimental benchmarks [9]. The electronic properties and band structure of the heterostructure were calculated using the *Nextnano* simulation suite. To accurately model the valence band structure and the hole-related transitions in the Ge/SiGe QWIP, we employed a 6-band $k \cdot p$ Hamiltonian [36] based on the Luttinger-Kohn formalization. While higher-order models (such as the 14-band $k \cdot p$ [37]) explicitly include conduction-valence coupling, the 6-band approach effectively incorporates the influence of these remote bands through the Luttinger parameters (γ_1, γ_2, γ_3). This formulation provides a rigorous description of the HH, light-hole (LH), and split-off (SO) dispersions, which is essential for calculating the ISBTs and the absorption spectra of p-doped QWIPs without unnecessary computational overhead.

The computational workflow is structured as follows:

1) Strain calculation: Since the MQW stack is coherently grown on a $Si_{0.2}Ge_{0.8}$ VS, the Ge wells undergo biaxial compression while the $Si_{0.3}Ge_{0.7}$ barriers experience tensile strain. These effects are incorporated through the Bir-Pikus Hamiltonian [38], which modifies the valence band edges and breaks the cubic symmetry. The strain-induced energy shifts at the Γ-point are determined by the hydrostatic deformation potential (a_v), which shifts the overall valence band position, and the shear deformation potential (b), which governs the splitting between the HH and LH subbands.
2) Potential profiling: The software solves the Poisson equation to account for the electrostatic potential induced by the boron doping spikes (2.5×10^{18} cm^{-3} to 5×10^{18} cm^{-3}) located at the center of the wells [39]. This self-consistent step ensures that the band-bending and charge redistribution are accurately captured.
3) Eigenvalue problem: Finally, the Schrödinger equation is solved at each k-point in the Brillouin zone. This allows for a precise mapping of the hole dispersion $E(k_{||})$ and the calculation of non-parabolic effective masses [26], both of which are critical for characterizing MIR transitions.

2.3. Many-body effects and optical absorption

To achieve an accurate description of the intersubband dynamics, this model accounts for many-body interactions, which become the dominant physical phenomena at the high doping densities investigated ($> 10^{18} cm^{-3}$, corresponding to a sheet density $> 10^{11} cm^{-2}$). At these concentrations, the holes confined within the Ge quantum wells form a two-dimensional hole

gas (2DHG), where collective interactions significantly alter the single-particle energy landscape. We implemented a self-consistent two-step correction to the Schrödinger-Poisson solution:

1) Exchange-correlation potential (V_{xc}): Calculated within the local density approximation (LDA) [40], this potential accounts for the many-body stabilization of the occupied ground state; the Gunnarsson-Lundqvist parametrization was adopted, which remains valid for holes by scaling the interaction strength with the appropriate effective masses. In the context of the 2DHG, V_{xc} represents the energy reduction due to the Pauli exclusion principle (exchange) and the avoidance of other holes due to Coulomb repulsion (correlation), resulting in a significant renormalization (red-shift) of the subband energies.
2) Depolarization shift: For TM-polarized ISBTs, we include the collective resonance effect. When excited by an external electromagnetic field, the 2DHG does not respond as a collection of independent particles, but as a single plasma-like entity. This collective oscillation of the hole gas perpendicular to the layers induces a time-dependent depolarization field [41, 42] that screens the external radiation. This effect results in a macroscopic restoration force that blue-shifts the absorption peak relative to the nominal single-particle energy separation, typically contributing up to 10% of the total transition energy.

Our results indicate that the dynamic depolarization blue-shift is the dominant mechanism, effectively over-compensating for the static V_{xc} red-shift and leading to the net blue-shift observed experimentally.

The optical absorption spectra were calculated by integrating the momentum matrix elements over the entire reciprocal space, specifically targeting the TM-polarized transitions between the ground state (*HH0*) and the first excited state (*HH1*). The model incorporates the complex non-parabolicity of the Ge valence band and temperature dependence via Fermi-Dirac statistics from 10 K to 300 K. To account for structural disorder and the finite lifetime of the excitations within the 2DHG, a phenomenological Lorentzian broadening was applied, incorporating alloy scattering and interface roughness parameters derived from the structural data.

2.4. Optoelectronic response and responsivity model

To evaluate the potential of the Ge/SiGe MQW as a Quantum Well Infrared Photodetector (QWIP), we developed a numerical model to estimate the spectral responsivity $R(\mathrm{k}\omega)$ [43]. Unlike purely analytical models, our approach utilizes the imaginary part of the dielectric function $\epsilon_2(\mathrm{k}\omega)$ extracted directly from the *Nextnano* 6-band $k \cdot p$ simulations. This quantity captures the complex valence band dynamics and the HH/light-hole mixing fundamental for describing the ISBT strength. The absorption coefficient $\alpha(\mathrm{k}\omega)$ was derived as:

$$\alpha(\hbar\omega) = \frac{\omega}{cn}\epsilon_2(\hbar\omega) \tag{2}$$

where $n = 3.84$ is the refractive index according to the formula [44],

$$\frac{4 \times 3nm + (3.42 + 0.37 \times 0.7 + 0.22 \times 0.7^2) \times 8nm}{11nm} = 3.84494 \tag{3}$$

So, we calculated the internal quantum efficiency (IQE) and the spectral responsivity, assuming an active region thickness of 700 nm (considering at a later stage 3 nm wells and 11 nm barriers) and an external quantum efficiency $\eta_{ext} = 0.6$. The resulting IQE of 0.11% is primarily a consequence of the single-pass normal-incidence geometry.

3. Results and Discussion

3.1. Valence band dispersion and the role of Luttinge parameters

To accurately describe the hole dynamics, our 6-band $k \cdot p$ model utilizes a curated set of Luttinger parameters (γ_1, γ_2, γ_3) (Figure 2) sourced from established Group-IV databases [45, 46]. Rather than treating these as static constants, our analysis highlights their critical role in governing the non-parabolicity and anisotropy of the valence bands. Specifically, the interaction between the HH and LH dispersions at non-zero transverse momentum ($k_{||} > 0$) leads to a profound band-mixing effect. We observe that the excited state 4⟩ (LH1 at Γ), which typically exhibits weak TM oscillator strength, acquires a significant HH character as $k_{||}$ increases. This redistribution of oscillator strength, captured through the $k \cdot p$ Hamiltonian, provides a rigorous physical explanation for the asymmetric spectral broadening observed in Sample B. This demonstrates that the 6-band formalism is essential to achieve quantitative agreement with experimental linewidths, surpassing the limitations of single-band effective mass models. For the $Si_{1-x}Ge_x$ alloy layers, the software automatically retrieves the endpoint values for pure Silicon and Germanium and applies a linear interpolation scheme—consistent with Vegard's Law—to determine the specific properties for any given Germanium mole fraction x. This systematic approach ensures that the strain-induced shifts and the valence band dispersion are calculated using a self-consistent and internationally recognized set of material descriptors.

Figure 2
Luttinger parameters γ_1, γ_2 and γ_3 obtained via band structure simulations based on the $k \cdot p$ method using the *Nextnano* software

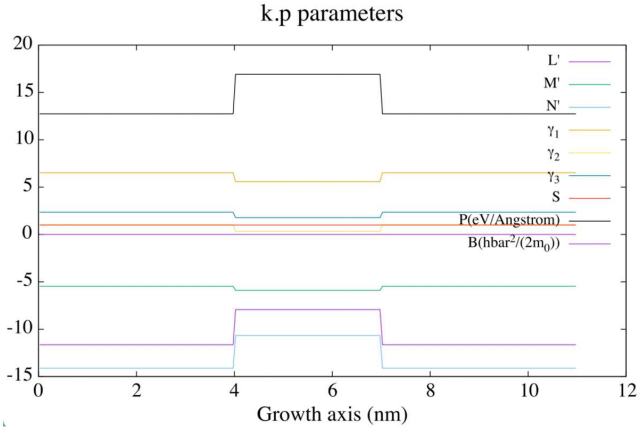

3.2. Strain-induced band splitting and polarization control

The epitaxial strain in Ge/SiGe quantum wells is a fundamental degree of freedom for tuning MIR optoelectronic responses. In our model, the strain state is determined by the

lattice mismatch between the $Si_{1-x}Ge_x$ layers and the $Si_{0.2}Ge_{0.8}$ virtual substrate. As shown in Figure 3, this strain reorders the valence band energetics at the Γ-point:

Figure 3
Valence band energy levels and corresponding wave functions at Γ also including above-band-edge levels at 300K for the Sample A

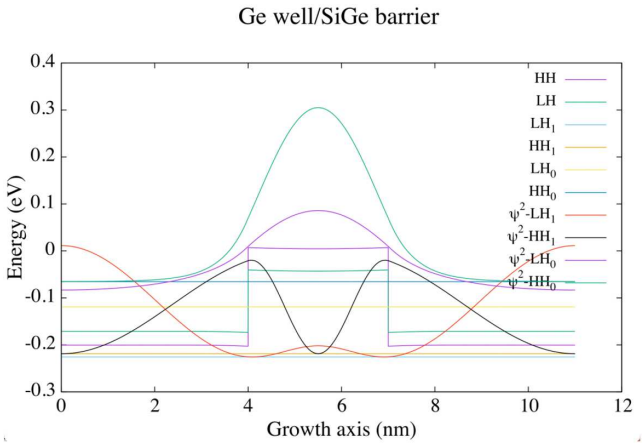

1) Compressive strain: In the Ge wells ($a_{layer} > a_{substrate}$), the HH subband is pushed above the Light Hole (LH) subband. This configuration enhances transitions interacting with TE-polarized light, which is critical for waveguide-integrated devices.
2) Tensile strain: Conversely, in the barriers, the LH band is promoted. By strategically engineering the barrier composition, we maximize the TM-matrix elements, optimizing the device for normal-incidence sensing.

3.3. Impact of many-body effects: Exchange-Correlation (LDA)

The precision of the peak position is highly sensitive to collective hole interactions. We performed a comparative analysis between "single-particle" solutions and those incorporating the LDA for the exchange-correlation potential (V_{xc}).

1) Redshift vs. blue-shift: While the Hartree potential (electrostatic repulsion) tends to broaden the well and decrease transition energy, the V_{xc} provides an attractive component for holes in the *HH*0 state, effectively deepening the potential well.
2) Density dependency: For the highly doped Sample B, the inclusion of V_{xc} results in a calculated blue-shift of approximately 8–12 meV compared to the bare Schrödinger-Poisson solution.
3) Experimental fit: When combined with the depolarization shift, the LDA-corrected model matches

The experimental TM-polarized dips (145–150 meV) with an accuracy of > 95%. Without these corrections, the model systematically underestimates the transition energy by approximately 10 meV, failing to replicate the experimental benchmarks and proving that many-body dynamics are fundamental components of MIR photonic design.

It is important to note that the 6-band $k \cdot p$ framework presented in this work provides the original theoretical basis for the results recently showcased in the work by Turpaud et al. [35]. While Turpaud et al. [35] utilized this specific model to validate experimental absorption dips (see Figure 7 in [35]), the present manuscript offers the first exhaustive disclosure of the underlying physics—including the self-consistent treatment of many-body effects and interface grading—which are inaccessible to simpler modeling approaches like tight-binding or effective mass approximations.

3.4. Role of band mixing and oscillator strength redistribution

A crucial finding of our 6-band $k \cdot p$ analysis concerns the nature of the excited states near the barrier edge. While single-band models treat transitions as independent and parabolic, the 6 × 6 Hamiltonian reveals a profound *HH-LH* band mixing induced by the non-zero transverse crystal momentum ($k_{||} > 0$). As k increases away from the Brillouin zone center (Γ), the wavefunctions undergo significant hybridization. Specifically, we observed that certain states, which exhibit weak TM oscillator strength at Γ, acquire a substantial HH component at higher $k_{||}$ values. This redistribution of oscillator strength provides a rigorous physical explanation for the asymmetric spectral broadening and the peak splitting observed in Sample B. As the chemical potential shifts deeper into the valence band due to high doping or elevated temperatures, these high-$k_{||}$ states become populated and optically active. This effect, uniquely captured by our formalism, allows for a quantitative agreement with experimental absorption profiles without the need for arbitrary empirical broadening factors.

3.5. Predictive tuning: Mapping the ISBT across the MIR window

We utilized the established framework to demonstrate the spectral tunability of the *HH0→HH1* transition. By performing a systematic sweep of the well thickness (L_w) from 2.5 nm to 5.5 nm, we show that the resonance peak can be precisely tuned across the 6–15 μm "fingerprint" region. Furthermore, by adjusting the Si content in the $Si_{1-x}Ge_x$ barriers, we can optimize the position of the excited state relative to the continuum. This "barrier engineering" is a critical factor for maximizing carrier extraction and responsivity in QWIP devices, ensuring that the design is not only theoretically sound but also electromagnetically optimized for target molecular sensing (e.g., CO_2 or CH_4 detection). The versatility of our model is further demonstrated by its ability to accurately predict transitions in complex potential profiles, such as the parabolic quantum wells recently reported in the work by Faverzani et al. [47]. Our framework remains the only one capable of describing the subband spacing in non-rectangular Ge/SiGe systems with quantitative precision, bridging the gap between growth and device design. Some of these results are shown in Figure 3.

The confined energy levels show an ISBT between the *HH0* and the *HH1* hole states of 154 meV and an ISBT between the LH0 and the LH1 holes states of 106 meV that agree respectively with the absorption in TM polarization and in TE polarization as shown in Figure 4 and the ratio in Figure 5.

Figure 4
Absorption coefficient versus energy for TM and TE polarization obtained with *Nextnano*

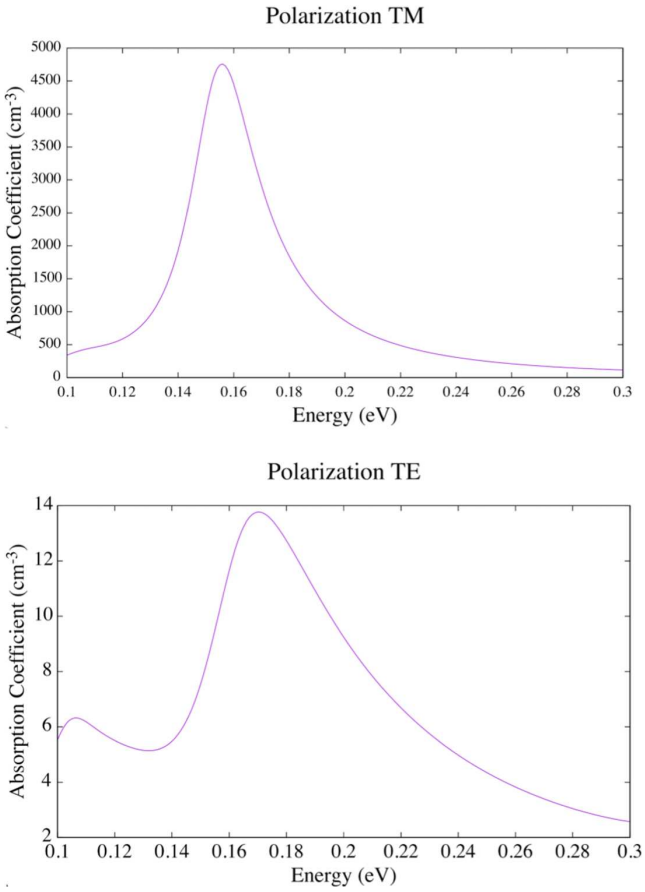

Figure 5
Ratio TM/TE

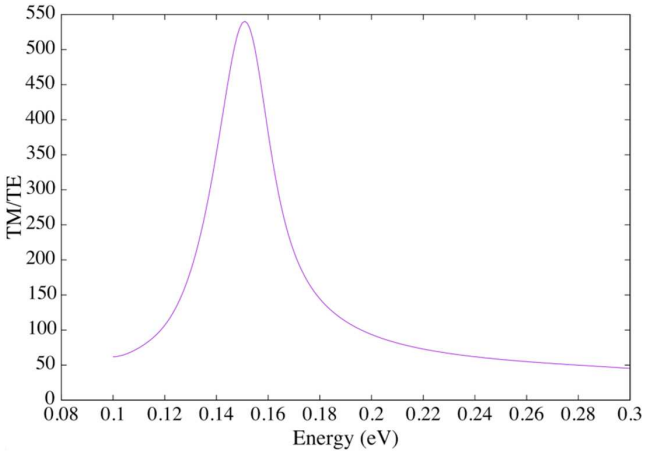

3.6. QWIP performance: Photocurrent and responsivity analysis

To bridge the gap between quantum simulations and practical sensing applications, we evaluated the optoelectronic response of the designed MQW structure. Starting from the imaginary part of the dielectric function $\epsilon_2(k\omega)$ extracted from *Nextnano*, the spectral absorption coefficient $\alpha(k\omega)$ was computed for a target photon energy of 0.150 eV (8.2 μm). Our model, implemented via a custom Python-driven workflow, estimates an IQE of 0.11%. While the single-pass absorption geometry results in a relatively low efficiency, the high oscillator strength of the Ge-rich wells yields a spectral responsivity R of 0.0042 A/W. Under a standard incident power density of 100 W/cm^2, the model predicts: Photocurrent Density: 424.81 mA/cm^2; Total Generated Photocurrent: 0.913 μA (for a device area of 0.0215 mm^2).

These results demonstrate that the p-doped Ge/SiGe platform is not only theoretically sound but also viable for practical MIR PIC sensors. The calculated responsivity provides a primary figure of merit that aligns our quantum-mechanical simulations with the experimental requirements for real-world molecular sensing. It is worth emphasizing that while preliminary estimations of responsivity in related experimental literature were obtained through decoupled, post-processing scripts, our model utilizes the full-device simulation capabilities of *Nextnano*. This allows for a self-consistent coupling between the quantum-mechanical absorption and the macroscopic carrier transport. Specifically, the photocurrent density reported here is generated within a unified solver, surpassing the accuracy of the fragmented computational routines used in previous material characterization studies. Please see the Supplementary Materials for more information.

4. Final Considerations and Future Research

4.1. Summary of the theoretical framework

The theoretical model developed in this study provides a robust first-order estimation of the photon-to-current conversion efficiency within the QWIP device. By utilizing realistic optical absorption data simulated via the *Nextnano* software framework, the model successfully bridges the gap between quantum-mechanical material properties and macroscopic measurable figures of merit. Specifically, the implementation allows for the direct computation of spectral responsivity and photocurrent, confirming that the device design is well-aligned with the target photon energy. This methodology offers a solid foundation for preliminary performance estimation, revealing the spectral profile and validating the underlying heterostructure design.

4.2. Current limitations

Despite its predictive utility, the present approach is subject to several simplifying assumptions that must be acknowledged. Primarily, the model assumes ideal carrier collection, effectively neglecting transport-related losses such as non-radiative recombination or carrier trapping. Furthermore, the external quantum efficiency (η_{ext}) is treated as a constant parameter, and the calculations do not currently account for optical reflection losses at the surface or the complex electrostatic effects at the metal-semiconductor contacts. The current model focuses on the optical generation rate but does not solve the coupled Poisson and drift-diffusion equations. Consequently, physical phenomena such as the influence of the internal electric field, carrier mobility, and the specific nature of the electrical contacts (whether Ohmic or Schottky) are not explicitly treated. These simplifications imply that the reported responsivity represents an upper theoretical limit—an optimistic estimate of the device's potential rather than a definitive quantitative prediction of experimental performance under bias.

4.3. Future work and advanced modeling

To refine the accuracy of these predictions, future research should transition from a purely optical-quantum model to a comprehensive electronic transport simulation. Integrating the current results with advanced computational methods would allow for the characterization of dark current, noise behavior, and bias-dependent responsivity. Two primary pathways are envisioned for this expansion: Drift-Diffusion Modeling: By numerically solving the continuity equations for electrons and holes alongside Poisson's equation, a more realistic current-voltage (IV) characteristic can be obtained, accounting for drift, diffusion, and recombination processes. Contact block reduction (CBR) Method: For a more rigorous quantum-mechanical treatment, the CBR method could be employed to simulate ballistic transport. This is particularly relevant for the quantized nature of the QWIP, where tunneling and quantum coherence significantly influence carrier extraction. In conclusion, while the current study provides a vital preliminary assessment of the QWIP's optical capabilities, the integration of a full electronic transport framework—incorporating contact boundary conditions and carrier dynamics—remains the necessary next step to fully characterize the operational performance of the device.

5. Conclusions

In this study, we presented a thorough theoretical analysis of p-doped Ge/SiGe MQWs for MIR photonics. By employing a self-consistent 6-band $k \cdot p$ model that integrates Bir-Pikus strain, graded interfaces, and many-body effects (LDA), we obtained a predictive design roadmap for *HH0→HH1* transitions in the 6–15 μm range. The high degree of agreement (> 95%) with experimental benchmarks confirms that our approach effectively overcomes the limitations of simplified effective mass models, established as a reliable tool for the ab-initio optimization of Si-based photodetectors. Future developments will extend this framework to model out-of-equilibrium transport and to index specific molecular resonances, such as CO_2 (4.26 mum) and CH_4 (7.7 μm), further bridging the gap between fundamental physics and practical environmental sensing.

Ethical Statement

This study does not contain any studies with human or animal subjects performed by the author.

Conflicts of Interest

The author declares that she has no conflicts of interest to this work.

Data Availability Statement

Data supporting the findings of this study are available from the corresponding author upon reasonable request.

Author Contribution Statement

Vittoria Urso: Conceptualization, Methodology, Software, Validation, Formal analysis, Investigation, Resources, Data curation, Writing – original draft, Writing – review & editing, Visualization, Supervision, Project administration.

Supplementary Materials

The supplementary materials are available from the article webpage at: https://doi.org/10.47852/bonviewJOPR62029098

References

[1] Tombez, L., Zhang, E. J., Orcutt, J. S., Kamlapurkar, S., & Green, W. M. J. (2017). Methane absorption spectroscopy on a silicon photonic chip. *Optica*, *4*(11), 1322–1325. https://doi.org/10.1364/OPTICA.4.001322

[2] Yallew, H. D., Vlk, M., Datta, A., Alberti, S., Zakoldaev, R. A., Høvik, J., . . . , & Aksnes, A. (2023). Sub-ppm methane detection with mid-infrared slot waveguides. *ACS Photonics*, *10*(12), 4282–4289. https://doi.org/10.1021/acsphotonics.3c01085

[3] Lin, H., Luo, Z., Gu, T., Kimerling, L. C., Wada, K., Agarwal, A., & Hu, J. (2018). Mid-infrared integrated photonics on silicon: A perspective. *Nanophotonics*, *7*(2), 393–420. https://doi.org/10.1515/nanoph-2017-0085

[4] Deckoff-Jones, S., Lin, H., Kita, D., Zheng, H., Li, D., Zhang, W., & Hu, J. (2018). Chalcogenide glass waveguide-integrated black phosphorus mid-infrared photodetectors. *Journal of Optics*, *20*(4), 044004. https://doi.org/10.1088/2040-8986/aaadc5

[5] Xia, L., Liu, Y., Chen, R. T., Weng, B., & Zou, Y. (2024). Advancements in miniaturized infrared spectroscopic-based volatile organic compound sensors: A systematic review. *Applied Physics Reviews*, *11*(3), 031306. https://doi.org/10.1063/5.0197236

[6] Butt, M. A., Juchniewicz, M., Słowikowski, M., Kozłowski, Ł., & Piramidowicz, R. (2025). Mid-infrared photonic sensors: Exploring fundamentals, advanced materials, and cutting-edge applications. *Sensors*, *25*(4), 1102. https://doi.org/10.3390/s25041102

[7] Mitchell, C. J., Hu, T., Sun, S., Stirling, C. J., Nedeljkovic, M., Peacock, A. C., . . . , & Rowe, D. J. (2024). Mid-infrared silicon photonics: From benchtop to real-world applications. *APL Photonics*, *9*(8), 080901. https://doi.org/10.1063/5.0222890

[8] Schliesser, A., Picqué, N., & Hänsch, T. W. (2012). Mid-infrared frequency combs. *Nature Photonics*, *6*(7), 440–449. https://doi.org/10.1038/nphoton.2012.142

[9] Dhote, C., Singh, A., & Kumar, S. (2022). Silicon photonics sensors for biophotonic applications—A review. *IEEE Sensors Journal*, *22*(19), 18228–18239. https://doi.org/10.1109/JSEN.2022.3199663

[10] Sajan, S. C., Singh, A., Sharma, P. K., & Kumar, S. (2023). Silicon photonics biosensors for cancer cells detection—A review. *IEEE Sensors Journal*, *23*(4), 3366–3377. https://doi.org/10.1109/JSEN.2023.3235920

[11] Zafar, H., & Pereira, M. F. (2024). Recent progress in light polarization control schemes for silicon integrated photonics. *Laser & Photonics Reviews*, *18*(11), 2301025. https://doi.org/10.1002/lpor.202301025

[12] Xiang, C., Jin, W., & Bowers, J. E. (2022). Silicon nitride passive and active photonic integrated circuits: Trends and prospects. *Photonics Research*, *10*(6), A82–A96. https://doi.org/10.1364/PRJ.452936

[13] Zhao, H., Zheng, C., Pi, M., Liang, L., Song, F., Zhang, Y., . . . , & Tittel, F. K. (2022). On-chip mid-infrared silicon-on-insulator waveguide methane sensor using two measurement

schemes at 3.291 μm. *Frontiers in Chemistry*, *10*, 953684. https://doi.org/10.3389/fchem.2022.953684

[14] Miloshevsky, A., Cohen, L. M., Myilswamy, K. V., Alshowkan, M., Fatema, S., Lu, H.-H., . . . , & Lukens, J. M. (2024). CMOS photonic integrated source of broadband polarization-entangled photons. *Optica Quantum*, *2*(4), 254–259. https://doi.org/10.1364/OPTICAQ.521418

[15] Marris-Morini, D., Mashanovich, G. Z., Nedeljkovic, M., Alonso-Ramos, C., Vivien, L., Frigerio, J., & Isella, G. (2026). Germanium-based mid-infrared integrated photonics. *Laser & Photonics Reviews*, *e017*(38). https://doi.org/10.1002/lpor.202501738

[16] Armand, R., Perestjuk, M., Campos, M. G. S., Chettri, U., Ferhat, L., Hartmann, J.-M., . . . , & Grillet, C. (2025). One million Q-factor SiGe-on-Si ring resonator in the mid-infrared. In *2025 Conference on Lasers and Electro-Optics Europe & European Quantum Electronics Conference*, 1. https://doi.org/10.1109/CLEO/Europe-EQEC65582.2025.11109834

[17] Della Torre, A., Sinobad, M., Armand, R., Luther-Davies, B., Ma, P., Madden, S., . . . , & Grillet, C. (2021). Mid-infrared supercontinuum generation in a low-loss germanium-on-silicon waveguide. *APL Photonics*, *6*(1), 016102. https://doi.org/10.1063/5.0033070

[18] Lim, J., Shim, J., Kim, I., & Kim, S. (2023). Experimental demonstration of high-Q MRR based on a germanium-on-insulator platform with an yttria insulator in the mid-IR range. *Photonics Research*, *11*(11), A80–A87. https://doi.org/10.1364/PRJ.495076

[19] Turpaud, V., Nguyen, T. H. N., Dely, H., Koompai, N., Bricout, A., Hartmann, J. M., . . . , & Marris-Morini, D. (2024). Low-loss SiGe waveguides for mid-infrared photonics fabricated on 200 mm wafers. *Optics Express*, *32*(10), 17400–17408. https://doi.org/10.1364/OE.521925

[20] Ballester, M. M. (2021). *SiGe photonics circuits exploit-ing nonlinear optics and electro-optic effects in the mid-infrared*. *PhD Thesis*. Université Paris-Saclay.

[21] Andresen, B. F., Fulop, G. F., & Zheng, L. (2022). *Infrared technology and applications XLVIII* (*12107*). USA: SPIE Digital Library.

[22] Fulop, G. F., Ting, D. Z., & Zheng, L. L. (2023). *Infrared technology and applications XLIX* (*12534*). USA: SPIE Digital Library.

[23] Xu, T., Dong, Y., Zhong, Q., Zheng, S., Qiu, Y., Zhao, X., . . . , & Hu, T. (2023). Mid-infrared integrated electro-optic modulators: A review. *Nanophotonics*, *12*(19), 3683–3706. https://doi.org/10.1515/nanoph-2023-0286

[24] Montesinos-Ballester, M., Deniel, L., Koompai, N., Nguyen, T. H. N., Frigerio, J., Ballabio, A., . . . , & Marris-Morini, D. (2022). Mid-infrared integrated electro-optic modulator operating up to 225 MHz between 6.4 and 10.7 μm wavelength. *ACS Photonics*, *9*(1), 249–255. https://doi.org/10.1021/acsphotonics.1c01449

[25] Du, J., Zhao, X., Miao, Y., Su, J., Duan, X., Dong, T., . . . , & Radamson, H. H. (2026). High-performance Ge-on-insulator photodetector enabled by thick Ge spacer and tensile-strained GeSi/Ge multiple quantum wells. *Optics Express*, *34*(5), 8067–8086. https://doi.org/10.1364/OE.584735

[26] Lodari, M., Kong, O., Rendell, M., Tosato, A., Sammak, A., Veldhorst, M., . . . , & Scappucci, G. (2022). Lightly strained germanium quantum wells with hole mobility exceeding one million. *Applied Physics Letters*, *120*(12), 122104. https://doi.org/10.1063/5.0083161

[27] Nigro, A., Vogel, A., Ruiz-Caridad, A., Weibel, V. J., Nieri Orfatti, D., Trautvetter, J., . . . , & Zardo, I. (2025). Strain engineering of Ge quantum wells in planar Ge/Si1-xGex heterostructures. *Advanced Materials Interfaces*, *12*(24), e00620. https://doi.org/10.1002/admi.202500620

[28] Xin, R., Li, N., Xia, H., Jiang, X., Yu, L., Liu, W., & Li, T. (2024). Probing electron density in quantum wells and its impact on the performance of infrared photodetectors. *IEEE Electron Device Letters*, *45*(10), 1740–1743. https://doi.org/10.1109/LED.2024.3439548

[29] Zhang, Y., Kong, Z., Sun, X., Li, J., Qin, Y., Wang, X., . . . , & Wang, G. (2026). Growth and quantum transport in sGe/GeO2 quantum wells. *ACS Applied Electronic Materials*, *8*(3), 1108–1118. https://doi.org/10.1021/acsaelm.5c02046

[30] Calcaterra, S., Faverzani, M., Impelluso, D., Chrastina, D., Giani, R., Anzi, L., . . . , & Frigerio, J. (2025). Optical and structural properties of p-doped Ge/SiGe multiple quantum wells for mid-infrared photonics. *Physical Review B*, *112*(4), 045429. https://doi.org/10.1103/9mm6-96nk

[31] Birner, S., Hackenbuchner, S., Sabathil, M., Zandler, G., Majewski, J. A., Andlauer, T., . . . , & Vogl, P. (2006). Modeling of Semiconductor Nanostructures with nextnano^3. *Acta Physica Polonica A*, *110*(2), 111–124. https://doi.org/10.12693/APhysPolA.110.111

[32] Lacerda-Santos, A., & Waintal, X. (2025). Electrostatics in semiconducting devices II: Solving the Helmholtz equation. *arXiv Preprint: 2507.03131*

[33] Botez, D., & Belkin, M. A (Eds.). (2023). *Mid-infrared and terahertz quantum cascade lasers*. UK: Cambridge University Press. https://doi.org/10.1017/9781108552066

[34] Sze, S. M., & Ng, K. K. (2021). *Physics of semiconductor devices* (4th ed.). USA: Wiley.

[35] Turpaud, V., Yang, Y., Dely, H., Bricout, A., Nguyen, T. H. N., El Bouchikhi, N., . . . , & Marris-Morini, D. (2025). Low-power supercontinuum generation in Ge-rich SiGe waveguides from 4 to 13 μm wavelength. *APL Photonics*, *10*(9), 090804. https://doi.org/10.1063/5.0270228

[36] Gladysiewicz, M., & Wartak, M. S. (2023). Analyzing k· p modeling in highly mismatched alloys and other III–V semiconductors. *Journal of Applied Physics*, *134*(23), 231101. https://doi.org/10.1063/5.0179100

[37] Zitouni, O., Saidi, H., & Ridene, S. (2024). Investigation of α-Sn dependence of band structure and optical emission in Si/SiyGe1-x-ySnx/Si quantum well laser. *Silicon*, *16*(8), 3573–3581. https://doi.org/10.1007/s12633-024-02928-7

[38] Zhang, S., He, Y., & Huang, P. (2023). Acceptor-based qubit in silicon with tunable strain. *Physical Review B*, *107*(15), 155301. https://doi.org/10.1103/PhysRevB.107.155301

[39] Tan, I.-H., Snider, G. L., Chang, L. D., & Hu, E. L. (1990). A self-consistent solution of Schrödinger–Poisson equations using a nonuniform mesh. *Journal of Applied Physics*, *68*(8), 4071–4076. https://doi.org/10.1063/1.346245

[40] Javed, A., Shaheen, M., Shahbaz, M., Ramzan, M. S., Ullah, R., & Jiang, W. (2025). Exchange-correlation functionals in 2D materials: Applications, challenges, and limitations. *arXiv Preprint: 2512.00921*

[41] Muravev, V. M., Andreev, I. V., Semenov, N. D., Gusikhin, P. A., & Kukushkin, I. V. (2024). Absorption of electromagnetic waves in a screened two-dimensional electron system. *Physical*

Review B, *110*(20), 205416. https://doi.org/10.1103/PhysRevB.110.205416

[42] Allen, S. J., Tsui, D. C., & Vinter, B. (1976). On the absorption of infrared radiation by electrons in semiconductor inversion layers. *Solid State Communications*, *20*(4), 425–428. https://doi.org/10.1016/0038-1098(76)90541-X

[43] Crisci, T., . Gioffrè, Moretti, L., M, & Casalino, M. (2022). Near-infrared schottky silicon photodetectors based on two dimensional materials. In M. Casalino & J. Thirumalai (Eds.), *Light-emitting diodes and photodetectors: Advances and future directions* (pp. 94–107). IntechOpen. https://doi.org/10.5772/intechopen.99625

[44] Levinshtein, M. E., Rumyantsev, S. L., & Shur, M. S. (2001). *Properties of advanced semiconductor materials: GaN, AIN, InN, BN, SiC, SiGe*. UK: John Wiley & Sons.

[45] Scheuler, N., Main, J., Rommel, P., Pfeiffer, F., Scheel, S., & Belov, P. A. (2026). Impact of the valence band on Rydberg excitons in cuprous oxide quantum wells. *Physical Review B*, *113*(11), 115413. https://doi.org/10.1103/1yqx-syzy

[46] Schäffler, F. (1997). High-mobility Si and Ge structures. *Semiconductor Science and Technology*, *12*(12), 1515–1549. https://doi.org/10.1088/0268-1242/12/12/001

[47] Faverzani, M., Impelluso, D., Calcaterra, S., Zucchetti, C., Chrastina, D., Tassi, C., . . . , & Frigerio, J. (2026). Mid-infrared intersubband transitions in p-type SiGe parabolic quantum wells. *Advanced Optical Materials*, *14*(3), e03060. https://doi.org/10.1002/adom.202503060

How to Cite: Urso, V. (2026). Band-Structure Engineering of P-Doped Ge/SiGe Heterostructures for Mid-infrared Photonic Devices. *Journal of Optics and Photonics Research*. https://doi.org/10.47852/bonviewJOPR62029098